

Ergodicity of gyrofluid edge localised ideal ballooning modes

J. Peer and A. Kendl

Institut für Ionenphysik und Angewandte Physik, Universität Innsbruck, Austria

B. D. Scott

Max-Planck-Institut für Plasmaphysik, Garching, Germany

Abstract

The magnetic field structure associated with edge localised ideal ballooning mode (ELM) bursts is analysed by nonlinear gyrofluid computation. The linear growth phase is characterised by the formation of small scale magnetic islands. Ergodic magnetic field regions develop near the end of the linear phase when the instability starts to perturb the equilibrium profiles. The nonlinear blow-out gives rise to an ergodisation of the entire edge region. The time-dependent level of ergodicity is determined in terms of the mean radial displacement of a magnetic field line. The ergodicity decreases again during the nonlinear turbulent phase of the blow-out in dependence on the degrading plasma beta in the collapsing plasma pedestal profile.

This is a preprint version of an article published in:

Plasma Physics and Controlled Fusion **55**, 015002 (2013).

I. INTRODUCTION

The steep gradients related to the edge transport barrier in tokamak H-mode plasmas facilitate the growth of edge localised modes (ELMs) involving repetitive eruption of particles and energy [1–3]. The largest and most vehement of such events, classified as “Type-I” ELMs, are commonly associated with the onset of ideal or peeling ballooning modes in edge pedestals [4–6].

In future large tokamak devices like ITER, the heat flux associated with type I ELMs is estimated to seriously damage the plasma facing components (PFCs) and methods for the suppression or at least effective mitigation of the disruptions are essential for an economic steady state operation [7–9]. One of the most promising ELM mitigation methods is the external application of resonant magnetic perturbations (RMPs) which has been observed to increase the ELM frequency and to reduce the heat load on the PFCs [10–13]. Models for the physics underlying the ELM mitigation by RMPs have been developed [6, 14, 15]. However, the successful mitigation even by nonresonant magnetic perturbations renews questions about the acting mechanisms [13].

Numerical computations are an important tool to analyse the physics and mode structure of ELMs. Ballooning ELM scenarios have been investigated in nonlinear simulations based on magnetohydrodynamic (MHD) [16–19], two-fluid [20, 21], and gyrofluid [22] models.

The magnetic structure has an essential part for development and transport of ELMs. In addition, numerical investigations of the interaction between ELMs and externally applied RMPs will require a detailed knowledge of the parallel mode structure and the resulting magnetic flutter associated with the ELM evolution in the perturbation-free case.

The present work focuses on nonlinear gyrofluid computation of the dynamical magnetic field structure associated with ideal ballooning ELMs. The formation of magnetic islands and the development of ergodic magnetic field regions, both observed in MHD simulations [16, 17], is reassessed with a gyrofluid code that in addition allows the consistent treatment of the small-scale turbulent blow-out [22–24].

It is found that an ideal ballooning ELM involves a distinct ergodisation of the entire edge region. The decrease of the ergodicity in the turbulent aftermath mainly depends on the evolution of plasma beta in the collapsing edge region.

The paper is organized as follows: In secs. II-IV, an overview of the model equations,

geometry and code is given, and suitable expressions for the evaluation of ergodicity in the numerical results are defined. The simulation setup and the model for the initial H-mode state are discussed in sec. V. The results for the ELM induced magnetic field structure and the associated formation of ergodic magnetic field regions are presented in secs. VI-VIII. In sec. IX, the results are summarized and discussed.

II. GYROFLUID ELECTROMAGNETIC MODEL AND GEOMETRY

The simulations presented in this work are performed with the nonlinear gyrofluid electromagnetic model and code GEMR [22]. In the following we review model equations and geometry.

GEMR includes six moment equations each for electrons and ions (labelled with $z \in \{e, i\}$), which are coupled by a polarisation equation and an induction equation [23]. The dependent variables are density n_z , parallel velocity $u_{z\parallel}$, parallel temperature $T_{z\parallel}$, perpendicular temperature $T_{z\perp}$, parallel component of the parallel heat flux $q_{z\parallel\parallel}$, perpendicular component of the parallel heat flux $q_{z\parallel\perp}$, electric potential ϕ , and parallel magnetic potential A_{\parallel} . The full set of model equations are treated in refs. [22, 23].

Here we use normalised quantities [23]: The perpendicular spatial scales are given in units of the minor plasma radius a . The time scale is normalised by a/c_{s0} , where $c_{s0} = \sqrt{T_{e0}/M_i}$ is a reference plasma sound speed. Here, M_i denotes the ion mass and T_{e0} is a reference electron temperature. The dependent variables are normalised by $n_z \leftarrow n_z/n_{z0}$, $T_z \leftarrow T_z/T_{z0}$, $u_{z\parallel} \leftarrow u_{z\parallel}/c_{s0}$, $q_{z\parallel} \leftarrow q_{z\parallel}/(n_{z0}T_{z0}c_{s0})$, $\phi \leftarrow (e\phi)/T_{e0}$, $A_{\parallel} \leftarrow A_{\parallel}/(\rho_{s0}\beta_{e0}B_0)$, where n_{z0} represents a reference density, T_{z0} is a reference temperature, e denotes the elementary charge, B_0 represents the equilibrium magnetic flux density, $\rho_{s0} = c\sqrt{M_i T_{e0}}/(eB_0)$ is the drift scale, and $\beta_{e0} = 4\pi p_{e0}/B_0^2$ is a reference value for the electron dynamical beta. Here, $p_{e0} = n_{e0}T_{e0}$ denotes the reference electron pressure. The magnetic flux density is normalised by B_0 .

The model dynamically evolves the full profiles of the dependent variables, where the inner (source) and outer (sink) radial boundaries are given by Neumann and Dirichlet conditions, respectively. The computational domain includes an edge pedestal closed-flux-surface region with consistent quasi-periodic parallel-perpendicular boundary conditions, and a scrape-off-layer (SOL) where the parallel boundary conditions represent a Debye sheath limiter placed

at the bottom side of a circular torus [25, 26].

The main model parameters are the electron dynamical beta β_{e0} , the normalised drift scale $\delta_0 = \rho_{s0}/a$, and the collisionality $\nu_{e0} = a/c_{s0}\tau_{e0}$, where τ_{e0} denotes a reference value for the Braginskii electron collision time [22, 23].

The evolution of the profiles is self-consistently coupled to the magnetic Shafranov equilibrium for circular flux surfaces. Both the safety factor q and the Shafranov shift are evolved in each time step [24].

The geometry is described in terms of field-aligned, unit-Jacobian Hamada coordinates (x, y_k, s) through

$$x = V = 2\pi^2 R_0 r^2, \quad (1)$$

$$y_k = y - \alpha_k = q\theta - \zeta - \alpha_k, \quad (2)$$

$$s = \theta \quad (3)$$

where V is the volume enclosed by the flux surface with major radius R_0 and minor radius r , and θ ($0 \leq \theta < 1$) and ζ ($0 \leq \zeta < 1$) are the unit-cycle poloidal and toroidal Hamada angles (see ref. [22] for their definition). V is given in units of a^3 , and R_0 and r are normalised by a . In order to avoid magnetic shear deformation of grid cells, the y -coordinate is shifted by $\alpha_k = q\theta_k + \Delta\alpha_k$, i.e. $\Delta\alpha_k$ is chosen to make ∇x and ∇y_k locally orthogonal at $\theta = \theta_k$ [27].

The initial magnetic equilibrium is computed from a prescribed safety factor profile $q_0(x)$. The temporal evolution of the Shafranov shift and $q(x)$ are determined by the Pfirsch-Schlüter current and the associated zonal ($m = n = 0$) component of A_{\parallel} . The change of $q(x)$ in each time step is given by [24]

$$\Delta \frac{1}{q} = -\frac{\delta_0 \beta_{e0} R_0}{r} \frac{\partial}{\partial r} \langle A_{\parallel} \rangle_{y,s} \quad (4)$$

where the brackets $\langle \dots \rangle_{y,s}$ denote the zonal average over y and s , and the factors δ_0 and β_{e0} enter due to the applied normalisation scheme. The Shafranov shift is incorporated into the coordinate grid by modifying the metric elements according to the s- α model. The resulting relevant part of the coordinate metric is given by

$$g^{xx} = \nabla x \cdot \nabla x = (V')^2 + \mathcal{O}(\varepsilon) = (2\pi)^4 (R_0 r)^2 + \mathcal{O}(\varepsilon) \quad (5)$$

$$g_k^{yy} = \nabla y_k \cdot \nabla y_k = \frac{q^2}{(2\pi r)^2} + \mathcal{O}(\varepsilon) \quad (6)$$

$$g_k^{xy} = \nabla x \cdot \nabla y_k = q'(\theta - \theta_k) - d'_s \sin(2\pi s) - \Delta\alpha'_k \equiv 0 \quad \text{at} \quad \theta = \theta_k \quad (7)$$

where the prime denotes a derivative with respect to r , g^{xx} and g_k^{xy} are given to lowest order in $\varepsilon = r/R_0$, and d'_s represents the local magnetic shear given by the Pfirsch-Schlüter current. In order to make g_k^{xy} locally vanish at $\theta = \theta_k$, the shift in the y -coordinate is defined as $\alpha_k = q\theta_k - d_s \sin \theta_k$, where d_s is given by

$$d_s = -\frac{\delta_0 \beta_{e0} q^2 R_0}{\pi r} \frac{\partial}{\partial r} \langle A_{\parallel} \cos(2\pi s) \rangle_{y,s} \quad (8)$$

The transformation ensures that magnetic field changes arising from the axisymmetric component of A_{\parallel} are placed on the coordinate grid. To avoid that this field component is considered twice, the axisymmetric part of A_{\parallel} is subtracted when the magnetic flutter is determined [24].

III. MAGNETIC FIELD STRUCTURE AND ERGODICITY

The focus of the present work is on the influence of edge localised ideal ballooning mode bursts on the magnetic field structure. The fluctuating magnetic potential enters into the macroscopic magnetic equilibrium through its zonal average via eq. 4 and sideband in eq. 8. The magnetic shear is accordingly determined by $\hat{s} = q'(r/q)$ and the Shafranov shift (eq. 8).

The perpendicular magnetic flutter, which enters into the parallel nonlinearities, results from the spatial variation of the non-axisymmetric part $\tilde{A}_{\parallel} = A_{\parallel} - \langle A_{\parallel} \rangle_y$ of the parallel magnetic potential. The magnetic fluctuations in direction of the perpendicular unit vectors $\hat{\mathbf{e}}^x$ and $\hat{\mathbf{e}}_k^y$ are given by

$$\hat{B}^x = \tilde{\mathbf{B}} \cdot \hat{\mathbf{e}}^x = \left(\nabla \times \tilde{\mathbf{A}} \right) \cdot \frac{\nabla x}{\sqrt{g^{xx}}} = \frac{\beta_{e0} \delta_0}{B^s \sqrt{g^{xx}}} \frac{\partial \tilde{A}_{\parallel}}{\partial y_k} \quad (9)$$

$$\hat{B}_k^y = \tilde{\mathbf{B}} \cdot \hat{\mathbf{e}}_k^y = \left(\nabla \times \tilde{\mathbf{A}} \right) \cdot \frac{\nabla y_k}{\sqrt{g_k^{yy}}} = -\frac{\beta_{e0} \delta_0}{B^s \sqrt{g_k^{yy}}} \frac{\partial \tilde{A}_{\parallel}}{\partial x} \quad (10)$$

where the factor $\beta_{e0} \delta_0$ results from the normalisation scheme. Eqs. 9 and 10 were derived by assuming $\tilde{\mathbf{A}} = A_{\parallel} \mathbf{b}$ and using the approximation $\nabla \times (A_{\parallel} \mathbf{b}) \approx -\mathbf{b} \times \nabla A_{\parallel}$, where $\mathbf{b} = \mathbf{B}/B$. The magnetic flutter field is divergence free in good approximation. For the present work the corrections resulting from the addition of lower order terms ensuring an exactly divergence free magnetic flutter field were found to be negligible.

The contravariant components of the magnetic flutter allow to evaluate the field line equation

$$\frac{B^x}{dx} = \frac{B_k^y}{dy_k} = \frac{B^s}{ds} \quad (11)$$

which will be used to visualize the magnetic field structure in terms of Poincaré plots.

Ergodic magnetic field regions develop when magnetic fluctuations destroy the nested magnetic equilibrium surfaces. The level of ergodicity can be measured by the average radial field line displacement defined by [28]

$$\sigma(r_0, l) = \frac{1}{N} \sum_{i=1}^N |r_i(l) - r_0| \quad (12)$$

where N denotes the number of considered field lines starting from a reference flux surfaces with radius $r = r_0$, l represents the length of a field line measured with respect to its starting point on the reference flux surface, and $r_i(l)$ gives the radial position of the i th field line after a length l .

IV. ADVECTIVE AND MAGNETIC TRANSPORT

Radial electromagnetic turbulent transport of heat and particles can occur by fluid-like perpendicular $E \times B$ advection, or through parallel motion along perpendicularly perturbed magnetic field lines. The differential formulation of the advective transport of ion density is given in field aligned coordinates by

$$dF_i^E = (n_i \mathbf{u}_E + T_{i\perp} \mathbf{w}_E) \cdot d\mathbf{S} = (n_i v_E^x + T_{i\perp} w_E^x) dy ds \quad (13)$$

where the area element $d\mathbf{S} = dy dy \nabla x$ is oriented in radial direction. $\mathbf{v}_E = \delta_0 \mathbf{b} \times \nabla \phi$ is the $E \times B$ velocity, and $\mathbf{u}_E = \delta_0 \mathbf{b} \times \nabla \phi_G$ and $\mathbf{w}_E = \delta_0 \mathbf{b} \times \nabla \Omega_G$ include the ion finite Larmor radius (FLR) corrected potentials $\phi_G = \Gamma_1 \phi$ and $\Omega_G = \Gamma_2 \phi$. The screening operators $\Gamma_2 = b(\partial \Gamma_1 / \partial b)$ for $b = k_\perp^2 \rho_i^2$ with $\Gamma_1 = \Gamma_0^{1/2}(b)$ are defined via the gyroaveraging operator Γ_0 [23]. The gyro averaging and screening operations are performed in Fourier space, and would in Padé approximation be given by $\Gamma_0^{1/2} \rightarrow (1 + b/2)^{-1}$. The advective electron heat transport is

$$dQ_e^E = (0.5 p_{e\parallel} + p_{e\perp}) \mathbf{v}_E \cdot d\mathbf{S} = (0.5 p_{e\parallel} + p_{e\perp}) v_e^x dy ds \quad (14)$$

where $p_{e\parallel} = n_{e\parallel} + T_{e\parallel}$ and $p_{e\perp} = n_{e\perp} + T_{e\perp}$ denote the linearised pressure in parallel and perpendicular direction, respectively.

The magnetic flutter transport of ion density is given by

$$dF_i^M = u_{i\parallel} \mathbf{b} \cdot d\mathbf{S} = u_{i\parallel} b^x dy ds, \quad (15)$$

where b^x denotes the radial component of the fluctuating magnetic field. Correspondingly, the magnetic flutter transport of electron heat is defined by

$$dQ_e^M = (q_{e\parallel\parallel} + q_{e\parallel\perp}) \mathbf{b} \cdot d\mathbf{S} = (q_{e\parallel\parallel} + q_{e\parallel\perp}) b^x dy ds. \quad (16)$$

The ion density transport in eq. 13 and 15 is normalised by $n_{i0}c_{s0}$. The electron heat transport in eq. 14 and 16 is given in units of $p_{e0}c_{s0}$.

V. MODEL FOR INITIAL H-MODE STATE

The onset of edge localised ideal ballooning modes is associated with the steep pressure gradient ($\alpha_M = q^2 R_0 |\nabla\beta| > \hat{s}$) in an H-mode pedestal. The present edge turbulence model – like any other available first-principles based model – is not able to obtain a self-sustained edge transport barrier with experimentally realistic steep flow and pressure profiles. In contrast to MHD models, the presence of the finite-beta ion-temperature-gradient instability at all values of beta and collisionality remove the familiar MHD threshold from the model. The H-mode edge state can however be prescribed as an initial condition, and the blow-out of one ideal ballooning event (destroying the transport barrier) can be computed from that. The procedure to obtain and start from such an initial H-mode like state with GEMR has been described in ref. [22].

The initial (reference) mid-pedestal values for density, temperature, and magnetic field are motivated by an exemplary ASDEX Upgrade H-mode shot (#17151) [29], and are given as $n_{e0} = n_{i0} = 2.5 \cdot 10^{19} \text{ m}^{-3}$, $T_{e0} = 300 \text{ eV}$, $T_{i0} = 360 \text{ eV}$, and $B_0 = 2 \text{ T}$. Major radius, minor radius, and gradient lengths for density and temperature correspond to $R_0 = 1.65 \text{ m}$, $a = 0.5 \text{ m}$, $L_n = 0.06 \text{ m}$, and $L_T = L_\perp = 0.03 \text{ m}$. The radial simulation domain has an extension of $\Delta r = 0.06 \text{ m}$ around the separatrix located at $r_0 = 1$, spanning both the pedestal and SOL regions. The initial q -profile is prescribed by $q_0 = 1.45 + 3.50 (r/r_0)^2$, which corresponds to a reference safety factor of $q_0(r_0) = 4.95$ and a reference magnetic shear of $\hat{s}_0(r_0) = 1.41$. The electron dynamical beta and the drift scale resulting from the local reference parameters are $\beta_{e0} = 4 \cdot 10^{-4}$ and $\rho_{s0} = 1.25 \cdot 10^{-3} \text{ m}$. The Braginskii electron collision time is $\tau_{e0} = 2.56 \cdot 10^{-6} \text{ s}$.

An evaluation of the MHD ballooning parameter gives $\alpha_M = q^2 R_0 |\nabla\beta_e| = 2.3 > \hat{s}_0$; thus the prescribed parameter set is expected to be ideal ballooning unstable. The Lundquist

number has the value $S = 4\pi v_A L / (c^2 \eta) = 4.5 \cdot 10^7$, where v_A is the Alfvén speed, $\eta = 0.51 m_e \nu_{e0} / (n_{e0} e^2)$ represents the plasma resistivity, and a characteristic length $L = R_0$ was assumed. The high Lundquist number indicates the possibility to include low- n ideal MHD modes [21].

The initial pedestal profiles for density $n(r) = (n_0/2)(L_\perp/L_n)g_0(r)$ and temperature $T(r) = (T_0/2)(L_\perp/L_T)g_0(r)$ are modelled by

$$g_0(r) = 1 - \sin\left(2\pi \frac{r - (r_0 - \Delta r/4)}{\Delta r}\right) \quad \text{for } r_0 - \Delta r/2 \leq r \leq r_0 \quad (17)$$

For pre-processing of the initial state a reduced grid resolution is used and the nonlinearities associated with the $E \times B$ advection and the parallel derivative are shut off, while the profiles are gradually ramped up [22]. A random turbulent pseudo-spectrum of density fluctuations with a relative amplitude of $a_0 = 10^{-4} \rho_{s0} / 2L_\perp$ was seeded on the background only inside the closed flux surface region. Excluding seeding on (and in the very vicinity of) the separatrix helps to reduce the onset spurious growth of ion temperature gradient (ITG) separatrix modes during the further (full scale) initial linear growth phase of the simulation. It was however found to be necessary to additionally pin the initial profiles of ion density and (thus cutting off neoclassical and parallel SOL transport around the separatrix) during the first stage of the ideal ballooning mode growth phase to completely avoid contamination by such unphysical separatrix ITG modes. As soon as the ballooning instability enters the nonlinear regime and starts to perturb the equilibrium quantities, all profiles are allowed to evolve self-consistently.

For this linear growth and nonlinear blow-out phase of the simulation a grid of $64 \times 512 \times 16$ points in radial (x), perpendicular (y) and parallel (s) direction is used. The resolution in (x, y) down to ρ_{s0} corresponding to $1.3 \cdot 10^{-3}$ m. The time step is set to $\Delta t = 0.002 a/c_s$, corresponding to $8.3 \cdot 10^{-9}$ s. Convergence during the MHD growth phase has been tested by doubling the space and time resolution, with a deviation of less than 5%.

VI. COMPUTATION OF DYNAMICAL MAGNETIC STRUCTURE

The rapid nonlinear transition from ideal ballooning mode to turbulent transport during a blow-out event has been characterised in ref. [22]. In the following the perturbed magnetic field structure of IBM bursts is analysed. Both the changes in the magnetic equilibrium

(i.e. the variation of the q -profile) and the magnetic flutter (i.e. the magnetic perturbations evolving from local current fluctuations) are considered.

Fig. 1 shows the time evolution of the density field $n_e(x, y)$ of an IBM blow-out in the outboard midplane at various times of the computation, starting from the initial conditions described above. At $t = 1$ ($\hat{=} 4 \mu\text{s}$) in fig. 1 (a) the fluctuations are randomly distributed within the closed flux surface region in the left half space of the (x, y) domain. The ballooning instability starts to grow where the pressure gradient is steepest, around $x \approx 61.3$. The linear growth phase, shown in (b) for $t = 18$ ($\hat{=} 75 \mu\text{s}$), is characterised by periodic density fluctuations with mode number $n = 6$. It is found that the dominant mode number depends on the pre-defined q -profile, but for various computations with different initial conditions the mode numbers all were in the range of $6 \leq n \leq 8$. After the peak growth phase nonlinear saturation takes over. Saturation occurs by energy transfer to drift-wave and ITG driven turbulence, which has been demonstrated in the fluctuation spectra shown in fig. 6 of ref. [22]. In (c) for $t = 24$ ($\hat{=} 100 \mu\text{s}$) the radial finger-like interchange density perturbations show their most marked appearance. In the turbulent aftermath, shown in (d) at $t = 51$ ($\hat{=} 210 \mu\text{s}$), the system transitions into a fully developed turbulent state with a mixed drift wave and ITG character. The MHD mode starts perturbing the profiles at $t \approx 21$ ($\hat{=} 88 \mu\text{s}$). The blowout phase (i.e. the induced erosion of density and temperature profiles) ends at $t \approx 40$ ($\hat{=} 170 \mu\text{s}$) and has thus a duration of about $80 \mu\text{s}$.

The effect of an IBM burst on the magnetic equilibrium ($n = 0$) structure is assessed via the change of the $q(x)$ -profile according to eq. 4. Fig. 2 shows the temporal evolution of changes in (a) safety factor ($q(x, t) - q_0(x)$), and (b) magnetic shear ($\hat{s}(x, t) - \hat{s}_0(x)$). Significant deviations from the initially prescribed values arise during the blow-out phase and persist in the turbulent aftermath.

The difference between the time dependent q -profile and the initial profile q_0 in (a) is in the range $-0.06 \leq (q - q_0) \leq 0.06$. The nonlinear growth phase is characterised by positive deviations in the central radial domain and negative deviations near both radial boundaries. In contrast, the turbulent aftermath exhibits positive deviations in the SOL and around the separatrix, and negative deviations in the closed field line region. The q -profile reflects the Shafranov shift: positive deviations from q_0 indicate a decreasing, negative deviations an increasing shift.

The deviations of the magnetic shear in (b) are in the range $-1.4 \leq (\hat{s} - \hat{s}_0) \leq 1.4$.

During the blow-out phase, the shear deviations are essentially positive in the closed field line region (except for the inner boundary) and essentially negative in the SOL. In the turbulent aftermath positive deviations dominate around the separatrix. The positive shear deviation until $t = 21$ is due to the local magnetic shear contribution (eq. 8) in the initial equilibrium state.

The equilibrium part of magnetic field changes has been determined by the Pfirsch-Schlüter current and the associated axisymmetric $n = 0$ toroidal mode number component of the parallel magnetic potential. The blowout reduces the Pfirsch-Schlüter equilibrium current by about 60%. Another contribution to the dynamical magnetic structure is due to the perpendicular magnetic perturbations resulting from the $n \geq 1$ components of A_{\parallel} . The time variation of this magnetic flutter is examined by evaluating eqs. 9 and 10. Figs. 3 and 4 show toroidal mode number spectra obtained from a Fourier transform of the magnetic flutter on the outboard midplane ($s = 0$).

The radial magnetic flutter $\hat{B}^x(x, t)$ in the $s = 0$ plane is shown in fig. 3 at various times, comparable to the evolution of structures in fig. 1. Initially at (a) $t = 1$ the perturbations extend over a broad spectrum including mode numbers in the range $2 \leq n \leq 20$ across the seeded confinement region. The linear growth phase at $t = 18$ in (b) is dominated by perturbations with mode number $n = 6$. The neighbouring mode with $n = 7$ is excited as well. The transition in (c) to nonlinear saturation at $t = 24$ involves a radial extension of the radial magnetic flutter, reflecting the formation of interchange fingers far into the SOL, and the second harmonic of the dominant mode becomes noticeably excited. In (d) the turbulent aftermath at $t = 51$ is characterised by nonlinear excitation of multiple modes distributed over a broad range of mode numbers. These signatures are also visible in the fluctuation spectrum as given in fig. 6 of ref. [22].

The evolution of the magnetic flutter component $\hat{B}_k^y(x, t)$ at $s = 0$, shown in fig. 4, is similar to that of \hat{B}^x . Remarkable differences concern the radial distribution of the perturbations during the (b) linear growth phase and (c) nonlinear blow-out phase, and the excitation of $n = 1$ modes during the blow-out phase and the turbulent aftermath in (d).

The amplitude of the magnetic flutter increases until the IBM instability saturates. The magnetic flutter is largest at $t = 25$, where $|\hat{B}^x| \approx |\hat{B}_k^y| \leq 10^{-2}$. The subsequent turbulent mixing involves a decrease of the magnetic perturbation level.

The magnetic flutter in the linear growth phase is also well characterised by the struc-

ture of the parallel current and the related parallel magnetic potential. Fig. 5 shows the fluctuations in the parallel current $J_{\parallel}(x, y)$, the related fluctuations in the parallel magnetic potential $\tilde{A}_{\parallel}(x, y)$, and the resulting magnetic flutter terms $\hat{B}^x(x, y)$ and $\hat{B}_k^y(x, y)$ in the outboard midplane during the linear growth phase at $t = 18$. The distinct periodic structure in J_{\parallel} , shown in (a), reflects the growth of the $n = 6$ density perturbation. The magnetic potential \tilde{A}_{\parallel} in (b) is coupled to the current through Ampère’s law. The resulting structure in both magnetic flutter components in (c) and (d) explains the radial distribution of the magnetic flutter found in fig. 3 (b) and 4 (b).

VII. MAGNETIC ISLANDS AND ERGODICITY

The periodic structure in the magnetic flutter leads to the question whether the linear growth of the IBM instability involves the formation of magnetic islands at resonant rational flux surfaces. Integrating eq. 11, the magnetic field structure can be visualised in terms of Poincaré sections. Fig. 6 shows Poincaré sections of the total simulation domain at two simulation times. For each plot, 160 field lines were traced over 4000 toroidal turns. Note that the requirement of a divergence-free magnetic field means that, despite the implemented limiter, the magnetic field lines in the SOL are closed. Hence, field lines can be traced over the entire radial simulation domain.

In the linear phase at $t = 18$, shown in fig. 6 (a), the magnetic flux surfaces in the closed-flux-surface region have an essentially laminar structure. Several chains of small scale magnetic islands with island widths $w \leq \rho_{s0}/2$ do not significantly perturb the flux surfaces. By contrast, applying the field line integration on the SOL (unphysically) exhibits larger, partly overlapping islands of widths $w \leq 3\rho_{s0}$. The largest islands in the SOL occur at rational surfaces with $6 \leq n \leq 7$ (i.e. at $q = 30/6, 36/7, 31/6, 32/6$) and are thus resonant with the linear IBM instability. The formation of magnetic islands in the SOL during the linear IBM growth phase is actually not physically reasonable. The computed large amplitudes of islands in the SOL are likely an artefact of the local δf model, which overestimates β and the electromagnetic response during the linear growth phase in the SOL (see sec. IX for a discussion on that point).

At the transition to the nonlinear phase at $t = 21$, shown in fig. 6 (b), most of the magnetic flux surfaces are destroyed and replaced by ergodic field regions. Note that the temporal

onset of ergodicity coincides with the formation of finger-like interchange perturbations.

Fig. 7 shows electron pressure contours in the poloidal plane. In the linear phase at $t = 18$, shown in fig. 7 (a), the iso-pressure surfaces coincide with the magnetic flux surfaces found in fig. 6 (a). At $t = 21$, the remaining laminar magnetic flux surfaces still follow the electron pressure. Hence, as long as the pressure fluctuations are small compared to the equilibrium profiles, the magnetic field satisfies the frozen-in condition of ideal MHD. As soon as nonlinear saturation takes over, resistive effects increase.

In order to quantify the time-dependent level of ergodicity, we evaluated the average radial displacement of a magnetic field line, as defined by eq. 12. Fig. 8 shows the time dependent average radial displacement of a magnetic field line after one toroidal turn in units of the drift scale ρ_{s0} . The average was formed by tracing 1000 field lines per flux surface. Fig. 8 (a) shows the displacement in dependence on radial coordinate and time. In fig. 8 (b) the average displacement in both closed-flux-surface region and SOL is plotted on a logarithmic scale. The linear growth phase is characterized by an exponential increase of the field line displacement. The maximum displacement of $\sigma \approx 4 \rho_{s0}$ coincides with the formation of the finger-like interchange perturbations at $t \approx 24$. Well after the ELM crash at $t = 50$, the displacement has reduced by 75 % with respect to its maximum value.

A comparison of the mean radial field line displacement with the Poincaré sections shown in fig. 6 shows that the IBM instability causes ergodic field regions if $\sigma \gtrsim 0.3 \rho_{s0}$. In the post-ELM turbulent phase for $t > 40$ a broad spectrum of modes contributes to the magnetic flutter and the threshold for magnetic ergodicity is lower. Indeed, the ELM blow-out induces an enduring ergodicity across the entire computation domain. Even at $t = 80$ ($\approx 200 \mu\text{s}$ after the ELM crash), where $\sigma \approx 0.2 \rho_{s0}$, most of the magnetic flux surfaces are destroyed.

Here, the question arises of whether the ergodicity of the magnetic field is even maintained in a saturated quasi L-mode-like post-ELM turbulent state. As the time scale of an ELM crash is much slower than the decrease of the profiles associated with the turbulent transport, the computation of the IBM blow-out was performed without density and heat sources. In the following we discuss a series of simulations including L-mode-like sources in the equations for density and temperature.

The reduced pedestal density and temperature in an L-mode or post-ELM state (compared to the H-mode transport barrier state) implies a reduction of the electron dynamical beta and the drift scale, and an increase of the electron collisionality. Accordingly, we

first investigated the scaling of the mean radial field line displacement with the free model parameters β_{e0} , ν_{e0} , and δ_0 . In a series of simulations, we varied β_{e0} , ν_{e0} , and δ_0 parameter-inconsistently, and evaluated σ for the respective saturated states. As the sources control the plasma fluctuation level, and consequently the amplitude of the magnetic flutter, the dependence on the magnitude of the source flux was investigated as well.

Fig. 9 (a) illustrates the scaling of the mean radial field line displacement with the electron dynamical beta β_{e0} , the electron collisionality ν_{e0} , the drift parameter δ_0 , and the source level S . Each point in the plot, represents an average over a time interval $\Delta t = 400$ ($\hat{=} 1.7$ ms). Except for the particular varied parameters and the addition of sources S^{nom} , the nominal parameters β_{e0}^{nom} , ν_{e0}^{nom} , and δ_0^{nom} correspond to those of the previous IBM case. The sources comprise a positive flux of density and heat acting near the inner radial boundary. The variation values of the free model parameters were selected according to their density and temperature dependence (i.e. $\beta_{e0} \propto n_{e0}T_{e0}$, $\nu_{e0} \propto n_{e0}T_{e0}^{-2}$, and $\delta_0 \propto T_{e0}^{1/2}$). We considered the cases with $n_{e0} = n_{e0}^{nom}$, $T_{e0} = T_{e0}^{nom}$ and $S = S^{nom}$ (parameter set P1), $n_{e0} = n_{e0}^{nom}/2$, $T_{e0} = T_{e0}^{nom}/2$ and $S = S^{nom}/2$ (parameter set P2), and $n_{e0} = n_{e0}^{nom}/4$, $T_{e0} = T_{e0}^{nom}/4$ and $S = S^{nom}/4$ (parameter set P3). The variation of the plasma parameters shown in fig. 9 (a) shows that σ decreases by 84% if the electron dynamical beta is decreased from $\beta_{e0} = \beta_{e0}^{nom}$ to $\beta_{e0} = \beta_{e0}^{nom}/16$. On the other hand, a decrease of the drift scale from $\delta_0 = \delta_0^{nom}$ to $\delta_0 = \delta_0^{nom}/2$ results in a increase of σ by 9%. The increase of the collisionality from $\nu_{e0} = \nu_{e0}^{nom}$ to $\nu_{e0} = 4\nu_{e0}^{nom}$ involves an insignificant decrease of σ by 1%. Finally, a reduction of the source flux from $S = S^{nom}$ to $S = S^{nom}/4$ results in an decrease of σ by 59%.

The above results indicate that the level of magnetic ergodicity is strongly influenced by the values of the local plasma parameters, especially by the plasma beta and the source level. A trend to lower ergodicity when going to L-mode-like values is indicated. In order to verify this trend in parameter-consistent simulations, we computed the mean radial field line displacement for parameter-consistent, saturated L-mode-like states characterized by the parameter sets P1, P2, and P3. Fig. 9 (b) shows that σ decreases by 88% if the reference values for density and temperature are parameter-consistently reduced to $n_{e0} = n_{e0}^{nom}/4$ and $T_{e0} = T_{e0}^{nom}/4$ and the source level is lowered from $S = S^{nom}$ to $S = S^{nom}/4$. Considering the Poincaré plots of the saturated state characterized by the parameter set P3, we find a slightly ergodized magnetic field. Thus, even L-mode-like turbulence can cause an ergodisation of

the magnetic field. Note that this ergodicity is dynamically evolving with the turbulence.

VIII. RADIAL TRANSPORT OF ION DENSITY AND ELECTRON HEAT

As the IBM blow-out involves a distinct ergodicity of the magnetic field, an increased magnetic transport of density and heat may be expected. In order to compare the magnetic transport (superscript M) with the $E \times B$ advective transport (superscript E), the ion density transport F_i and the electron heat transport Q_e are analysed. The motivation for considering F_i instead of F_e is that the bulk of mass is transported by the ions. On the other hand, the higher mobility of the electrons implies that $Q_e^M \gg Q_e^E$, so that only Q_e is of interest.

Fig. 10 shows the volume averaged transport quantities F_i^M , F_i^E , Q_e^M and Q_e^E for both closed-flux-surface region and SOL. The ion density transport shown in (a) and (b) is clearly dominated by $E \times B$ advection. The ratio between magnetic transport and $E \times B$ transport is less than 10^{-2} , and the only relevant magnetic contributions are restricted to the time interval $25 \lesssim t \lesssim 45$ around and shortly after the peak IBM mode phase.

In contrast, the electron heat transport shown in (c) and (d) exhibits a significant magnetic component. In the closed-flux-surface region after the peak IBM mode phase for times $t \gtrsim 25$, the ratio between average magnetic and advective electron heat transport is between the values $0.2 \leq \langle Q_e^M \rangle_{x,y,s} / \langle Q_e^E \rangle_{x,y,s} \leq 0.8$. The magnetic transport in the SOL is by approximately one order of magnitude smaller than in the closed-flux-surface region so that the ratio $\langle Q_e^M \rangle_{x,y,s} / \langle Q_e^E \rangle_{x,y,s}$ has values around 0.1 in the SOL.

In the case of a saturated L-mode-state based on plasma parameters which reflect post-ELM conditions (reduced plasma beta and drift parameter, increased electron collisionality), the magnetic transport of electron heat is, on average, by two orders of magnitude lower than the $E \times B$ advective transport. Likewise, the magnetic density transport is by three orders of magnitude smaller than the $E \times B$ transport. Thus, the only regime where the magnetic transport substantially contributes to the total transport, is the peak IBM mode phase and the following transition to a turbulent state at times $24 \lesssim t \lesssim 40$.

The time-dependent total ELM energy loss, quantified by the loss fraction of the equilibrium pedestal energy $W_{ped} = 3/2(p_e + p_i)$, is shown in fig. 11. At $t = 40$, which can be considered as the end of the ELM crash, the energy loss amounts to about 42%. At

that time, the average pedestal density of both electrons and ions has dropped by 41 % with respect to the initial equilibrium state. The electron temperature at $t = 40$ has decreased by half and the ion temperature by a third. As the advective transport of electron and ion heat is nearly equal in magnitude, the larger decrease of the electron temperature compared to the ion temperature can be ascribed to the additional magnetic transport which is negligibly small for the ions.

IX. SUMMARY AND DISCUSSION

The magnetic field structure associated with edge localised ideal ballooning mode (IBM) bursts was investigated computationally using the nonlinear gyrofluid electromagnetic model GEMR. The simulation setup was geared to exemplary ASDEX Upgrade H-mode conditions. Both the IBM induced changes in the magnetic equilibrium and the magnetic flutter due to local plasma fluctuations were investigated. The formation of magnetic islands and ergodic magnetic field regions was visualized by Poincaré sections. In order to discuss the level of magnetic ergodicity associated with the IBM blow-out and the subsequent turbulent aftermath, the average radial displacement of a magnetic field line was evaluated. The level of ergodicity was investigated for several saturated turbulent states in which the electron dynamical beta, the electron collisionality, the drift scale and the magnitude of the source flux were varied. Furthermore, the mean radial field line displacement was evaluated for parameter-consistent, saturated L-mode-like states. Finally, the volume averaged magnetic transport of ion density and electron heat was compared to the corresponding $E \times B$ transport and the total ELM energy loss was discussed.

The main results can be summarized as follows:

1. The IBM induced changes in the safety factor profile amount up to 1 % of the initially prescribed value q_0 ($0.99 \lesssim q(x)/q_0(x) \lesssim 1.01$). Due to the spatial variation of the safety factor profile (short-scale transitions from negative to positive deviations) and the additional local shear piece resulting from the Shafranov shift, the corresponding changes in the magnetic shear amount up to 100 % of the initially prescribed value \hat{s}_0 ($0 \lesssim \hat{s}(x)/\hat{s}_0(x) \lesssim 2$).
2. The time-dependent toroidal mode number spectra of both perpendicular magnetic

flutter components reflect the evolution of the initially dominant $n = 6$ mode. The different spatial variation of the magnetic flutter components is due to the structure in the pressure fluctuations and the related current fluctuations. The magnitude of the magnetic flutter increases until the IBM instability nonlinearly saturates ($|\hat{B}^x| \approx |\hat{B}_k^y| \lesssim 10^{-2}$).

3. The linear growth of the IBM instability involves the formation of small scale magnetic islands in the closed-flux-surface region ($w \leq \rho_{s0}/2$). The laminar structure of the magnetic surfaces in the closed-flux-surface region is not significantly perturbed. The formation of resonant magnetic islands in the SOL can be ascribed to the use of a local δf model, which implies that the electromagnetic response in the SOL during the linear growth phase is highly overestimated.
4. Ergodic magnetic field regions form near the end of the linear phase when the IBM instability starts to perturb the equilibrium profiles.
5. The level of magnetic ergodicity (measured by the average radial field line displacement) increases until the IBM instability saturates. The turbulent aftermath of the burst results in an enduring ergodicity across the simulation domain.
6. Even in a saturated turbulent L-mode-like post-ELM state the magnetic field remains ergodized. However, the level of ergodicity decreases if the plasma parameters are adjusted to the reduced post-ELM profiles.
7. The IBM induced magnetic transport of ion density can be neglected in comparison to the corresponding $E \times B$ transport. By contrast, the magnetic transport of electron heat can amount up to 80% of the corresponding $E \times B$ transport. The magnetic transport of electron heat is significant during the blow-out phase and the subsequent transition to a turbulent state. In a saturated L-mode-like post ELM state the magnetic contribution to the electron heat transport is negligibly small.
8. The total pedestal energy loss of the IBM burst amounts to about 40% of the equilibrium pedestal energy.

Considering these points we can conclude that the ideal ballooning ELM scenario involves an enduring ergodisation of the entire edge region. Moreover, the L-mode like post-ELM

state is also characterized by a non vanishing degree of magnetic ergodicity.

For correct interpretation of the results we have to discuss several limitations of the present local (“ δf ”) turbulence model. The code GEMR evolves the profiles as part of the dependent variables but the derivation of the model equations is based on local parameters. The discrepancy between radially varying profiles and inconsistent local plasma parameters increases with the distance from the flux surface for which the plasma parameters were defined. This implies that especially in the SOL the deviation from the consistent plasma parameters is large.

For the simulations presented in this work this means that the plasma beta is unrealistically high when considering the range around the separatrix and the SOL. Hence, the electromagnetic response and, in particular, the magnetic flutter are overestimated in the SOL. Especially during the linear growth phase of the IBM instability, where the profiles in the SOL are close to zero, the plasma beta in the SOL is highly overestimated as self-consistent values would be close to zero. The formation of resonant magnetic islands and ergodic field regions in the SOL during the linear growth phase can be ascribed to this model inconsistency.

The discrepancy between profiles and plasma parameters also concerns the transition from the peak IBM blow-out phase resulting from H-mode-like plasma parameters to an L-mode-like turbulent post-ELM state which is characterized by a decreased plasma beta. We have shown that the mean radial field line displacement decreases up to one order of magnitude if the nominal simulation parameters are changed to describe a saturated L-mode-like post-ELM state.

Our results that the magnetic heat transport during the ELM crash and the subsequent turbulent state is always smaller than the heat transport by $E \times B$ advection seems to disagree with the fact that the magnetic field is ergodized at all times during and after the ELM blow-out. This apparent contradiction can be solved by comparing the radial $E \times B$ velocity with the radial velocity associated with the motion of an electron along a perturbed magnetic field line. Considering the mean radial field line displacement after one toroidal turn and assuming an electron moving with thermal velocity, we find that the average radial velocity associated with the magnetic flutter during and after the peak blow-out phase is about one order of magnitude smaller than the radial $E \times B$ velocity. Hence, the magnetic fraction of the electron heat transport can be small although the magnetic field is ergodised.

The point is that the magnetic flutter and the resulting ergodicity is continuously changing with time such that an electron within one simulation time step sees only a fraction of the magnetic snapshot visualized in a Poincaré plot. Thus, an ergodic region in a Poincaré plot is not necessarily indicative of a dominant magnetic transport.

The ELM induced ergodicity of the magnetic field was earlier investigated by MHD simulations [16–18]. While MHD models more readily allow for the implementation of a realistic X-point-geometry, the present gyrofluid simulations (including turbulent scales) are based on a simplified circular geometry. Still, the present results regarding the ELM induced formation of an ergodic edge region as well as the associated magnetic transport are in qualitative agreement with MHD results. In the present GEMR modelling the major novel results concern the small-scale dominated turbulent aftermath immediately following the IBM burst.

Acknowledgments

We thank T.T. Ribeiro for valuable discussions on the model, code and results, and F.P. Genrich for routines for preparation of the initial state. This work was partly supported by the Austrian Science Fund (FWF) Y398; by the Austrian Ministry of Science BMWF as part of the UniInfrastrukturprogramm of the Forschungsplattform Scientific Computing at LFU Innsbruck; and by the European Commission under the Contract of Association between EURATOM and ÖAW carried out within the framework of the European Fusion Development Agreement (EFDA). The views and opinions expressed herein do not necessarily reflect those of the European Commission.

References

- [1] Zohm H, Plasma Phys. Control. Fusion 38, 105, 1996.
- [2] Connor J W, Plasma Phys. Control. Fusion 40, 531, 1998.
- [3] Becoulet M et al, Plasma Phys. Control. Fusion 45, A93, 2003.
- [4] Snyder P B et al, Phys. Plasmas 9, 2037, 2002.
- [5] Wilson H R et al, Plasma Phys. Control. Fusion 48, A71, 2006.
- [6] Snyder P B et al, Nucl. Fusion 47, 961, 2007.
- [7] Federici, G. and Loarte, A. and Strohmayer, G., Plasma Phys. Control. Fusion 45, 1523, 2003.
- [8] Loarte, A. and Saibene, G. and Sartori, R., et al. Plasma Phys. Control. Fusion 45, 1549, 2003.
- [9] Federici, G., Phys. Scr. T124, 1, 2006,
- [10] Evans, T. E. and Moyer, R. A. and Watkins, J. G. , et al., Nucl. Fusion 45, 595, 2005.
- [11] Evans, T. E. and Moyer, R. A. and Burrell, K. H., Nat. Phys. 2, 419, 2006.
- [12] Liang, Y. and Koslowski, H. R. and Thomas, P. R., et al., Phys. Rev. Lett. 98, 265004, 2007.
- [13] Suttrop, W. and Eich, T. and Fuchs, J. C., et al., Phys. Rev. Lett. 106, 225004, 2011.
- [14] Tokar, M. Z. and Evans, T. E. and Gupta, A. and Singh, R. and Kaw, P. and Wolf, R. C., Phys. Rev. Lett. 98, 095001, 2007.

- [15] Tokar, M. Z. and Evans, T. E. and Gupta, A. and Kalupin, D. and Nicolai, A. and Singh, R. and Unterberg, B., Nucl. Fusion 48, 024006, 2008.
- [16] Huysmans, G. T. A. and Czarny, O., Nucl. Fusion 47, 659, 2007.
- [17] Huysmans, G. T. A. and Pamela, S. and van der Plas, E. and Ramet, P., Plasma Phys. Control. Fusion 51, 124012, 2009.
- [18] Sugiyama, L. E. and Strauss, H. R., Phys. Plasmas 17, 062505, 2010.
- [19] Pamela, S. J. P. and Huysmans, G. T. A. and Beurskens, et al., Plasma Phys. Control. Fusion 53, 054014, 2011.
- [20] Xu, X. Q. and Dudson, B. and Snyder, P. B. and Umansky, M. V. and Wilson, H., Phys. Rev. Lett. 105, 175005, 2010.
- [21] Dudson, B. D. and Xu, X. Q. and Umansky, M. V. and Wilson, H. R. and Snyder, P. B., Plasma Phys. Control. Fusion 53, 054005, 2011.
- [22] Kendl, A. and Scott, B. D. and Ribeiro, T. T., Phys. Plasmas 17, 072302, 2010.
- [23] Scott B D, Phys. Plasmas 12, 102307, 2005.
- [24] Scott B D, Contrib. Plasma Phys. 46, 714, 2006.
- [25] Ribeiro T T and Scott B, Plasma Phys. Control. Fusion 47, 1657, 2005.
- [26] Ribeiro T T and Scott B, Plasma Phys. Control. Fusion 50, 055007, 2008.
- [27] Scott B, Phys. Plasmas 8, 447, 2001.
- [28] Finken K H et al, Nucl. Fusion 39, 637, 1999.
- [29] Horton L D et al, Nucl. Fusion 45, 856, 2005.

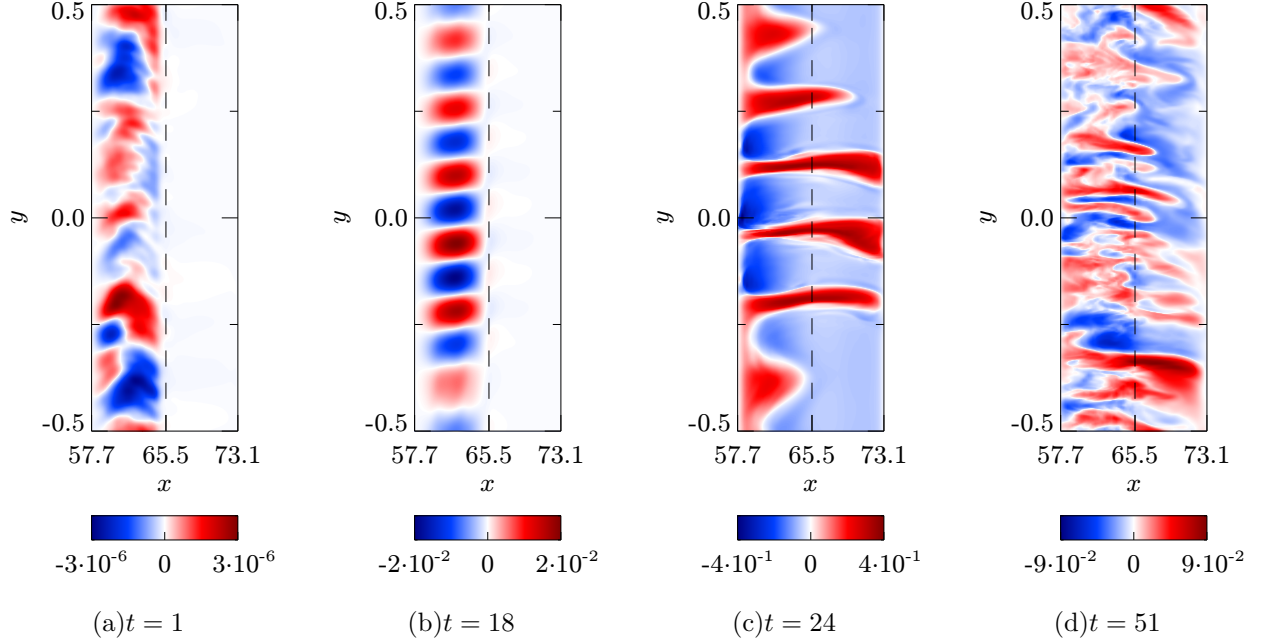


FIG. 1: (Colour online) Time evolution of an ideal ballooning mode burst illustrated by snapshots of electron density fluctuations in the outboard midplane ($s = 0$). For visualisation of fluctuations the toroidal mean has been subtracted as $\tilde{n}_e = n_e - \langle n_e \rangle_y$. The dashed lines mark the separatrix. Time and space scales are given in normalised units.

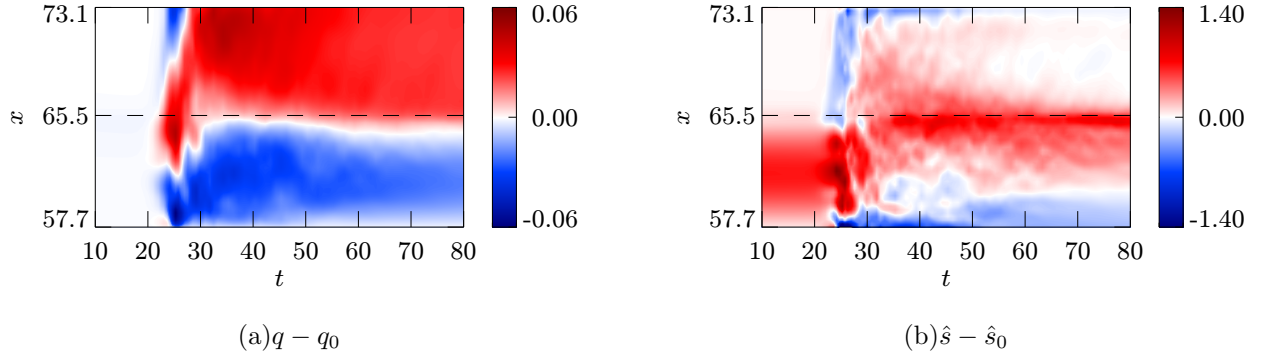


FIG. 2: (Colour online) Ideal ballooning ELM induced changes in the magnetic equilibrium. The deviation of (a) the safety factor profile q from the initially prescribed profile q_0 and (b) the corresponding deviation of the magnetic shear \hat{s} from the initial shear \hat{s}_0 are shown. The dashed lines mark the separatrix. Time and space scales are given in normalised units.

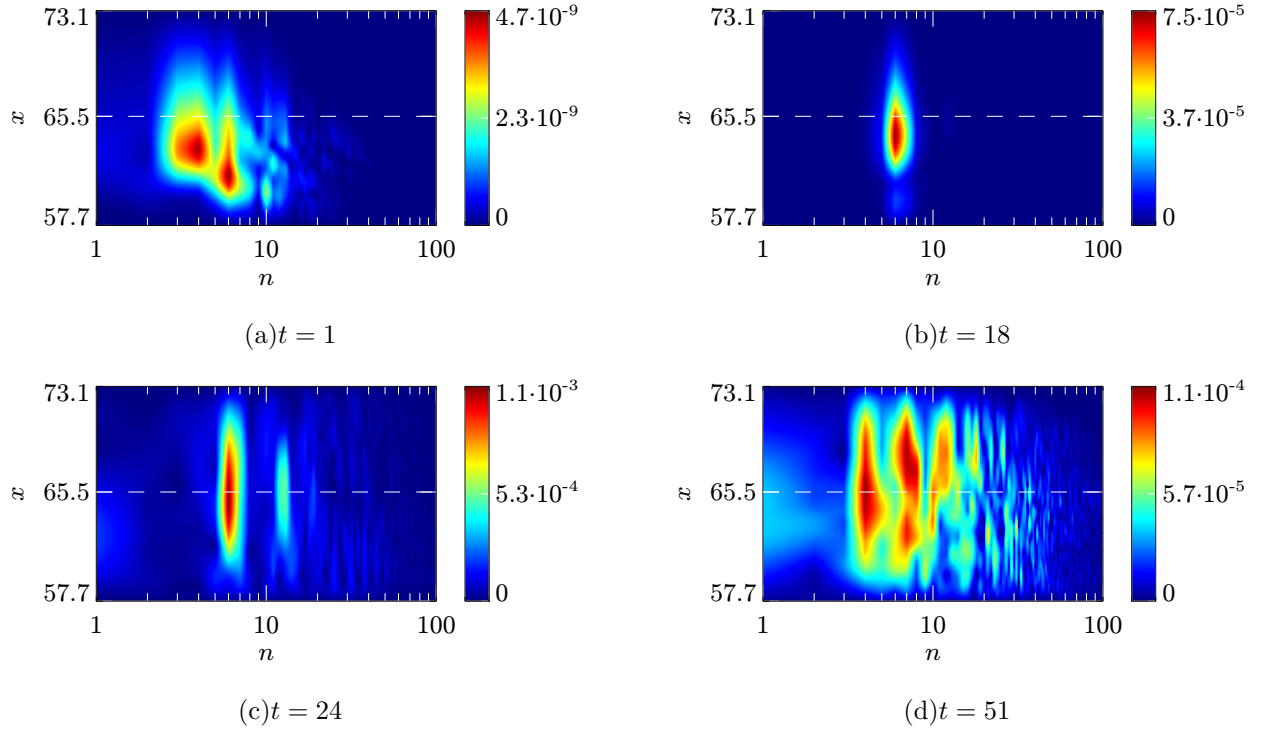


FIG. 3: (Colour online) Time evolution of magnetic flutter \hat{B}^x . Toroidal mode number spectra in the outboard midplane ($s = 0$) are shown at various times. The dashed lines mark the separatrix. Time and space scales are given in normalised units.

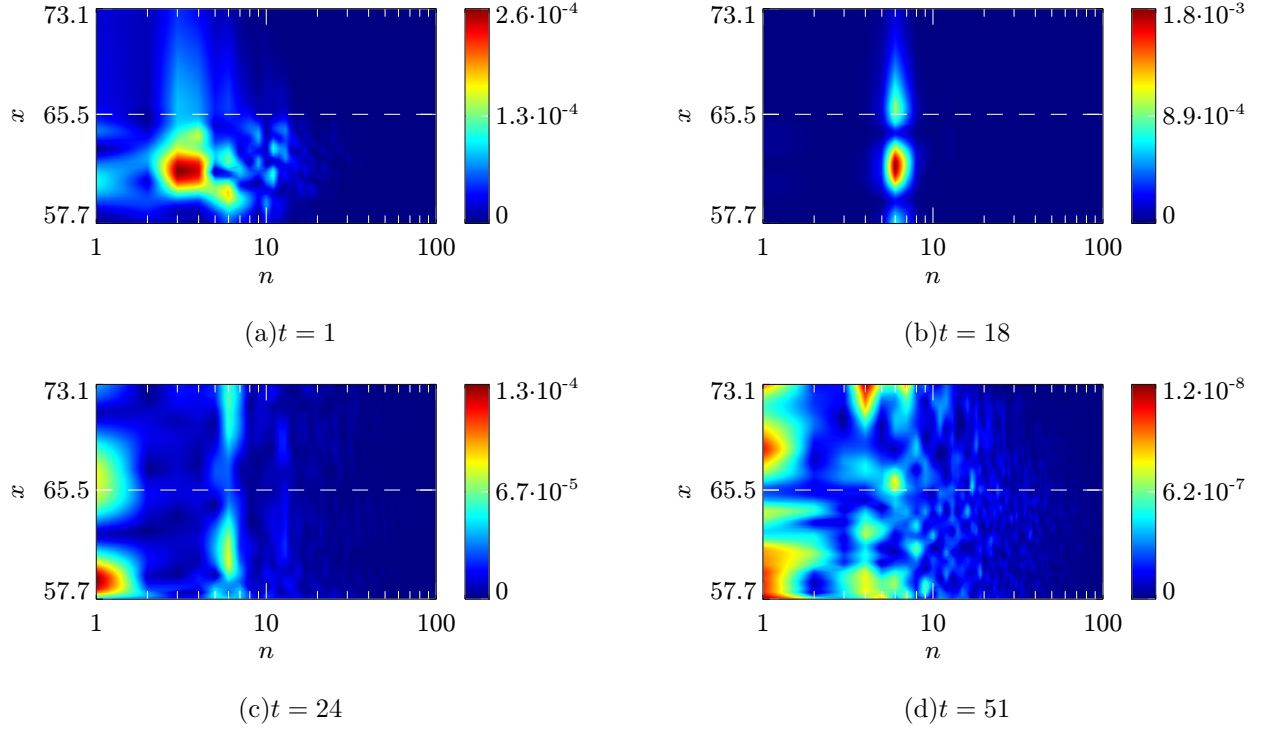


FIG. 4: (Colour online) Time evolution of magnetic flutter \hat{B}_k^y . Toroidal mode number spectra in the outboard midplane ($s = 0$) are shown at various times. The dashed lines mark the separatrix. Time and space scales are given in normalised units.

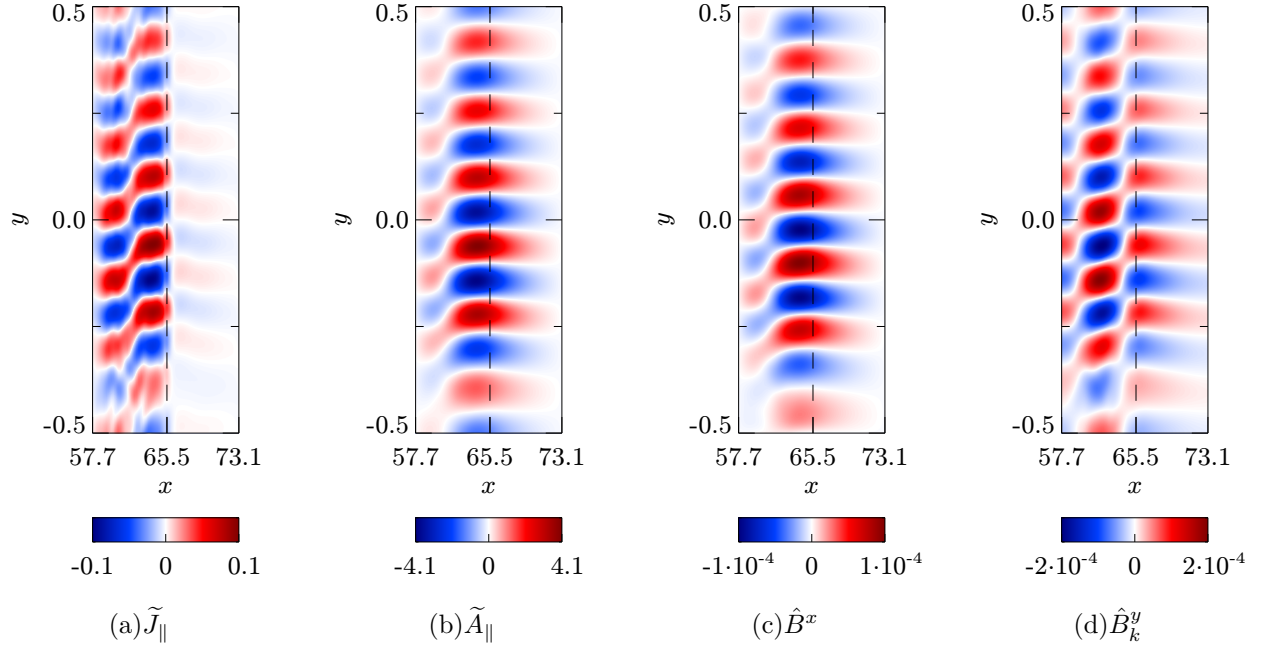
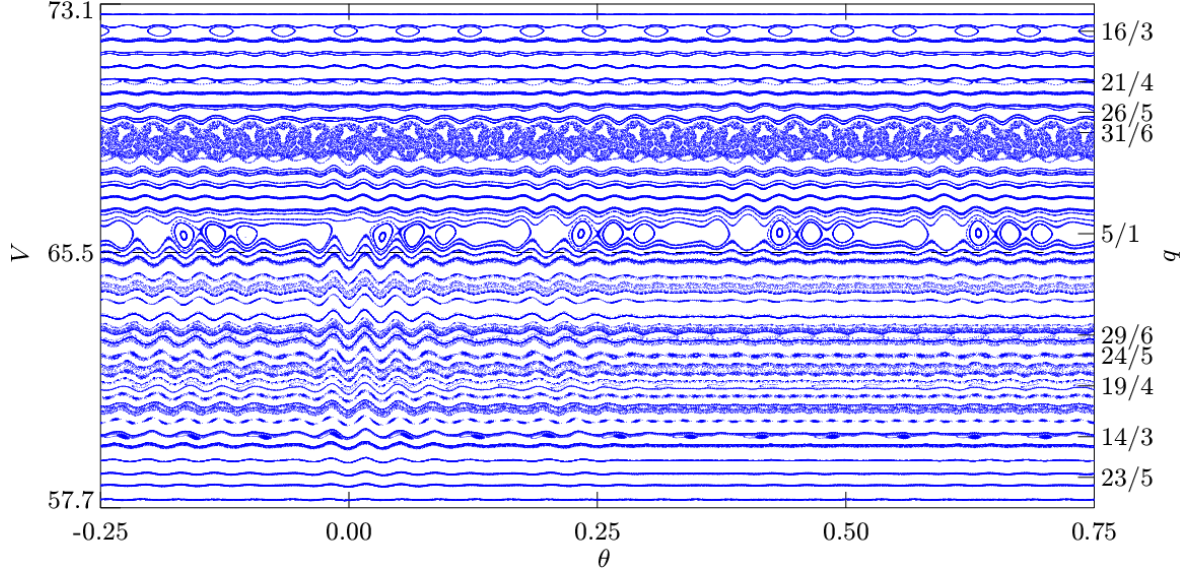
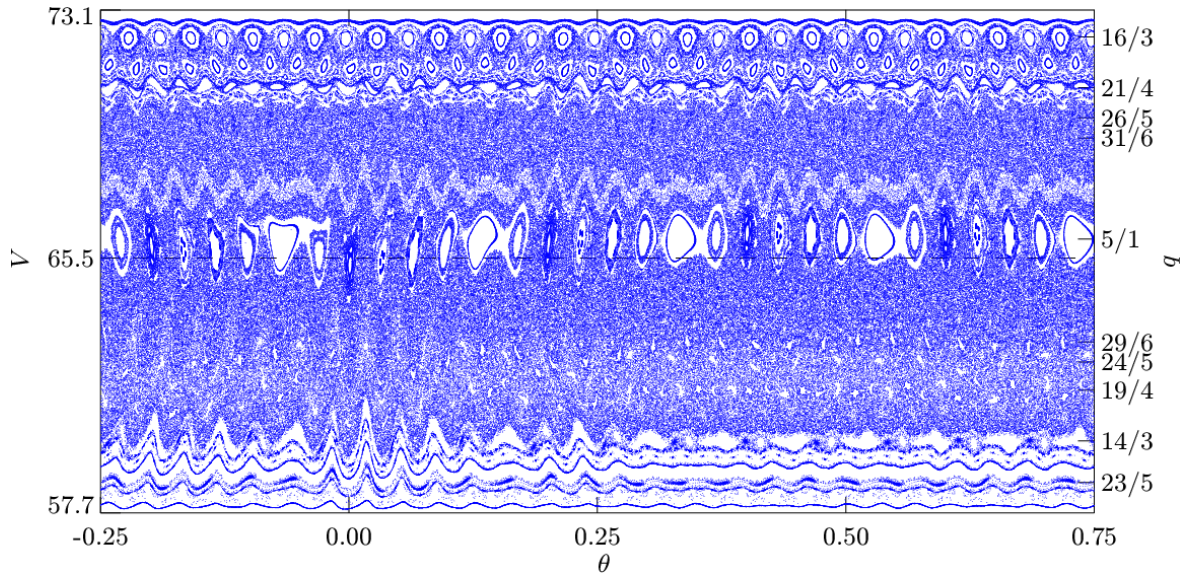


FIG. 5: (Colour online) Fluctuations in (a) the parallel current and (b) the parallel magnetic potential, and the resulting (c, d) perpendicular magnetic flutter associated with the linear IBM growth phase at $t = 18$. Fluctuations are shown by subtracting the toroidal mean ($\tilde{J}_{\parallel} = J_{\parallel} - \langle J_{\parallel} \rangle_y$, $\tilde{A}_{\parallel} = A_{\parallel} - \langle A_{\parallel} \rangle_y$). The dashed lines mark the separatrix. Time and space scales are given in normalised units.



(a) $t = 18$



(b) $t = 21$

FIG. 6: Poincaré sections of the magnetic field lines illustrating the IBM induced transition from laminar magnetic flux surfaces at (a) $t = 18$ to evolving ergodicity at (c) $t = 21$. The dashed lines mark the separatrix. Time and space scales are given in normalised units.

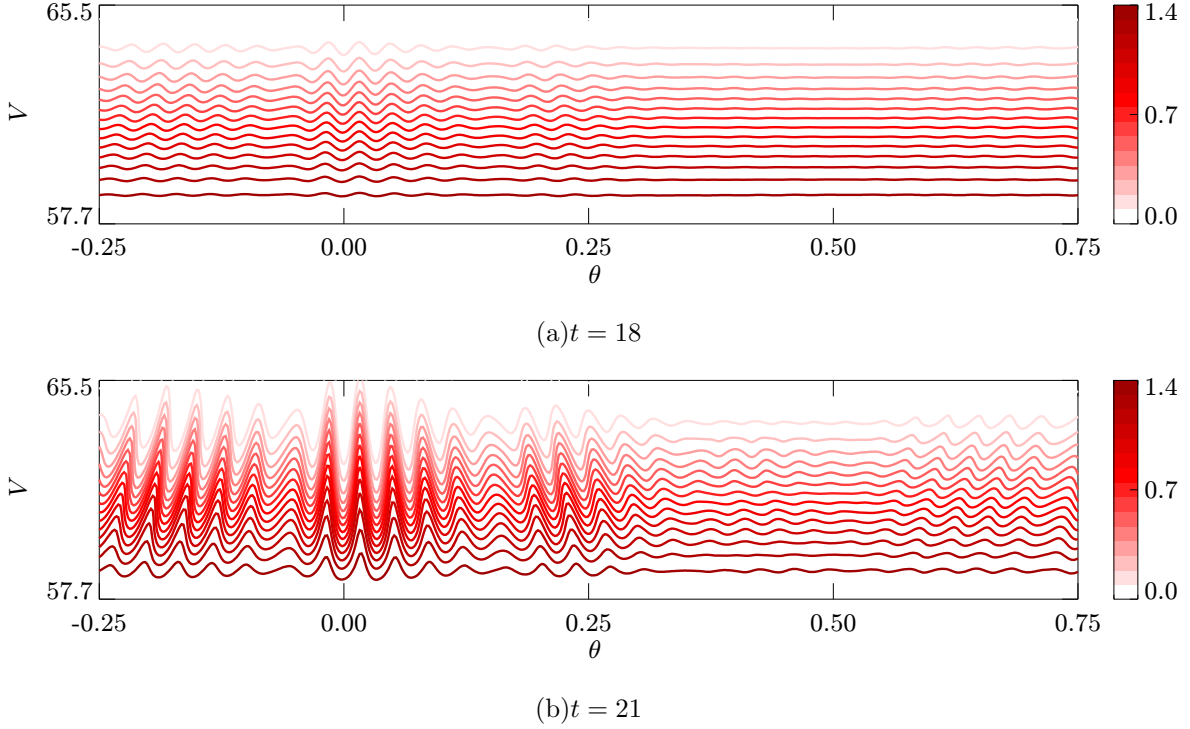


FIG. 7: Electron pressure contours in the poloidal plane. The closed-flux-surface region of figs. 6 (a,b) is shown. Time and space scales are given in normalised units.

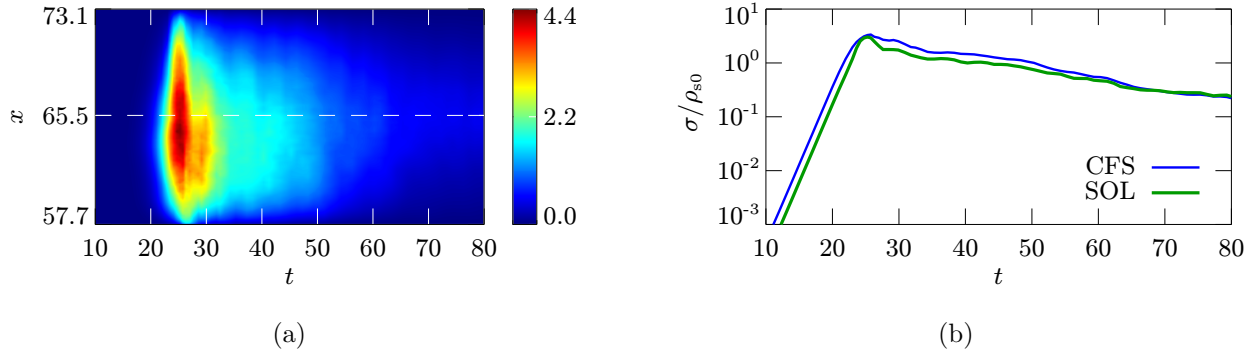
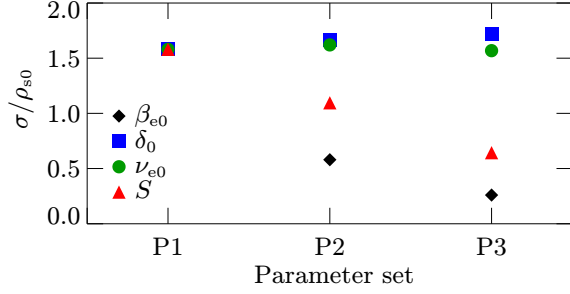
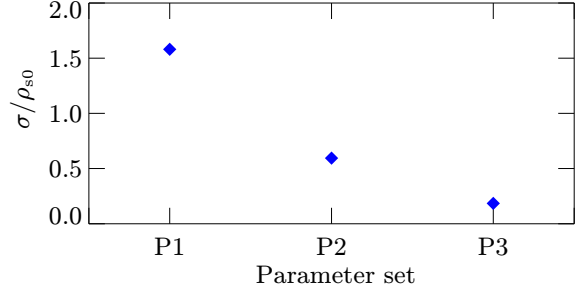


FIG. 8: (Colour online) Mean radial field line displacement in units of the drift scale after one toroidal turn. The (a) radial variation on a linear colour scale and (b) the radially averaged displacement on a logarithmic scale is shown for the closed-flux-surface (CFS) and the scrape-off-layer (SOL) region. The dashed line marks the separatrix. Time and space scales are given in normalised units.

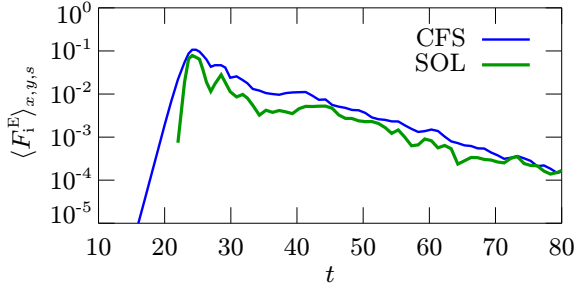


(a) Inconsistently varied parameters

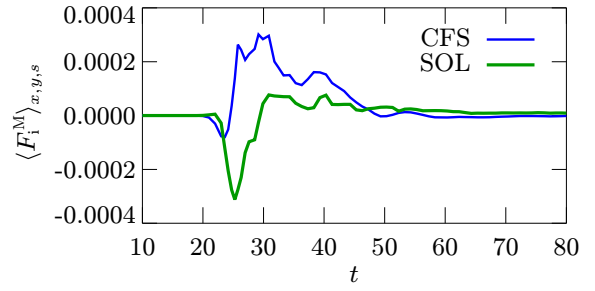


(b) Self-consistently varied parameters

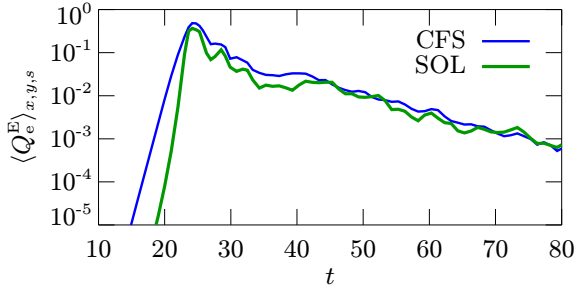
FIG. 9: Scaling of the mean radial field line displacement with the plasma beta β_{e0} , the drift parameter δ_0 , the electron collisionality ν_{e0} , and the source level S . Each point represents the average over a saturated turbulent L-mode-like state. The parameter set P1 corresponds to the nominal parameters. In P2 and P3, the parameters were computed from one half and one fourth of the nominal density and temperature profiles, respectively. For (a) only one parameter was inconsistently varied, (b) shows parameter consistent simulations. See text for details.



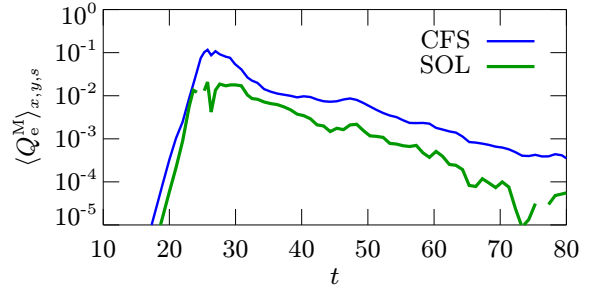
(a)



(b)



(c)



(d)

FIG. 10: Ideal ballooning ELM induced, volume averaged radial transport of (a,b) ion density and (c,d) electron heat. The (a,c) $E \times B$ advective transport is compared to the (b,d) parallel magnetic transport. Closed-flux-surface (CFS) and scrape-off-layer (SOL) region are separately shown. Time and transport are given in normalised units.

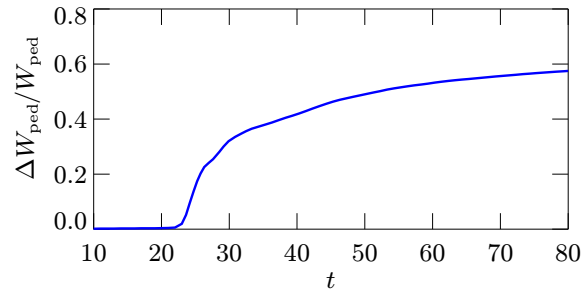


FIG. 11: Ideal ballooning ELM induced loss of pedestal energy with respect to the equilibrium pedestal energy. The time is given in normalised units.